

Graphene-Encapsulated Nitrogen-doped Carbon@Bi Enables Rapid, Ultrahigh and Durable Sodium Storage

Meixue Wang,^[a] Huijun Li,^[a] Xiaoqin Cheng,^[a] Shizhen Tian,^[a] and Xiaomin Wang^{*[a]}

Bismuth (Bi) has promising applications as anode in sodium-ion batteries (SIBs) due to its suitable alloy voltage, unique lattice structure and high volumetric specific capacity. However, the severe structural degradation and poor cycling performance of Bi-anode during cycling limits its practical application. Here, we designed and synthesized graphene-encapsulated nitrogen-doped carbon@bismuth (N-C@Bi/G) composites as anode materials for SIBs by a two-step hydrothermal and thermal treatment method to solve the above problems. The N-C@Bi/G composite anode material exhibits excellent sodium storage performance, high capacity (280 mAh g⁻¹ at 0.1 A g⁻¹) and an

initial coulombic efficiency of 78.87%) and long-term cycling stability (260 mAh g⁻¹ after 1000 cycles at 2 A g⁻¹). Electrochemical analysis and DFT calculations show that the fast reaction kinetics of N-C@Bi/G is directly related to the introduction of nitrogen-doped carbon enriching the pore structure and increasing the active sites. Meanwhile, through the aid of in-situ X-ray diffraction (XRD), the reaction mechanism and interphase evolution of N-C@Bi/G composite are revealed, which provides an important theoretical basis for the application of SIBs.

Introduction

The rapid depletion of fossil energy sources has led to the rapid development of renewable energy sources such as tidal energy and solar power, however, the unsustainability of these sources requires efficient and cost-effective energy storage systems.^[1] Although lithium-ion batteries are currently the dominant device, the limited resources of lithium have limited their further large-scale application.^[2] In recent years, sodium-ion batteries (SIBs) are of great interest in large-scale energy storage applications. Compared with lithium-ion batteries, sodium-ion batteries have more advantages in terms of their abundant and environmentally friendly sodium ion content, long cycle life, high multiplier performance, low cost and high safety.^[3] While some notable progress has been made with SIBs, there are still problems that constrain its practical applications. For example, low energy density, poor rate performance and cyclic stability. It is a key challenge to design an anode material with excellent sodium ion storage properties compatible with existing electrolytes, positive electrodes,^[4] which have a significant impact on the output voltage, energy density and stability of sodium-ion batteries.

Depending on the storage mechanism of sodium, anode materials for SIBs can be broadly classified into three categories: intercalation, conversion and alloy-based anode materials.^[5] Since the radius of Na⁺ (1.02 Å) is significantly larger than that of Li⁺ (0.76 Å), it is difficult for Na⁺ to insert between commercial graphite layers, resulting in a lower

theoretical capacity (358 mAh g⁻¹) and lower energy density.^[6] In addition, although transition metal oxides/sulfides based on the conversion reaction mechanism have higher capacities, their high platform voltage (~1.5 V) and poor cycle stability still limit their practical applications.^[7] Therefore, alloyed anodes (Sn, Sb, Bi, P, etc.) have received increasing attention in recent years due to the possibility of forming sodium-rich alloys with suitable sodicity potentials (0.3–1.0 V vs. Na⁺/Na) and high specific capacities (300–2000 mAh g⁻¹).^[8]

Bismuth (Bi) due to its suitable alloying voltage (\approx 0.6 V vs. Na⁺/Na)^[9] and a special layered structure (along the c-axis direction, $d(003)=3.95\text{ \AA}$)^[10] considered as a promising anode material for SIBs. These features allow Bi to store sodium ions (volume capacity of 3800 mAh cm⁻³) more easily by means of alloying/dealloying reaction. Also, NaBi and Na₂Bi have an embedding process during the phase transition to accommodate more Na⁺, which suggests that the Bi negative electrode has the potential to exceed its theoretical capacity (385 mAh g⁻¹).^[11] However, Bi also has common problems of alloy-based negative electrodes, with dramatic volume expansion/contraction during charging and discharging, leading to the chalking of the negative electrode and the generation of an unstable solid electrolyte interface (SEI), which allows for rapid capacity decay.^[12] By designing nanostructures, Liu et al. used chemical dealloying to synthesize one-dimensional nanorods stacked into arrays of Bi bundles, which, thanks to their nanostructure, exhibited good electrochemical performance as a sodium ion anode material, with capacity maintained at 301.9 mAh g⁻¹ after 150 cycles at 50 mA g⁻¹.^[8a] Using conductive composites, Xiang et al. prepared by a self-templating method to obtain two-dimensional carbon-coated Bi nanoplates (Bi@C), in which the two-dimensional carbon nanosheets served to limit the volume expansion of Bi during sodium embedding while improving the electrical conductivity of the material.^[8b] Methods such as the formation of alloys or

[a] M. Wang, Dr. H. Li, Dr. X. Cheng, S. Tian, Dr. X. Wang
College of Materials Science and Engineering
Taiyuan University of Technology
Tai Yuan Shi, 030024 (PR China)
E-mail: wangxiaomin@tyut.edu.cn

 Supporting information for this article is available on the WWW under
<https://doi.org/10.1002/batt.202300055>

intermetallic compounds to improve the electrochemical properties of Bi anodes have received extensive attention. For example, Guo et al. prepared a lattice-softened antimony-bismuth alloy/carbon nanofiber (SbBi_3/C), which enhanced cycling stability by adjusting the lattice chemistry of the rhombic bimetallic alloy to give the alloy a lower elastic modulus and higher Poisson's ratio, enhancing a stronger fracture toughness to withstand the large volume change during cycling.^[13]

Currently, porous carbon materials are receiving much attention as it provides a larger surface for the dispersion of Bi nanoparticles and further facilitates electron transfer and ion diffusion in a larger space.^[14] Su et al. reported Bi@graphene composites with a sodium storage capacity of 361 mAh g^{-1} , but the life is extremely short (50 cycles);^[10a] Li et al. reported a Bi nanosphere/porous carbon (Bi/C) composite with a retention capacity of only 106 mAh g^{-1} after 1000 cycles.^[15] Overall, these Bi-based anode materials still face large capacity degradation over long cycles, especially at high current densities, where the carbon layer is destroyed. Therefore, Bi nanoparticles are encapsulated in a more stable and intact carbon matrix, is essential to achieve long cycle stability at high current densities.^[14a,16]

Herein, a graphene-encapsulated nitrogen-doped carbon@bismuth(N–C@Bi/G) was designed and synthesized in this paper, which was prepared by a two-step hydrothermal method and annealing treatment. The nitrogen-doped carbon layer (N–C) with abundant defects provides more surface ion storage active sites and reduces ion/electron diffusion pathways, which can improve the reaction kinetics. The three-dimensional interconnected graphene network provides a larger surface for the dispersion of N–C@Bi nanoparticles, which can further facilitate electron transfer and ion diffusion in a larger space and enhance the storage performance. As expected, the prepared electrode materials exhibit high capacity (309 mAh g^{-1} at 0.1 A g^{-1}) and excellent rate performance and long-term cycling stability (up to more than 1000

cycles at 2 A g^{-1}). In addition, electrochemical analysis provides insight into the mechanism of action of the nitrogen-doped carbon. Moreover, the structural evolution of N–C@Bi/G during the sodium storage has been investigated in depth in combination with in-situ X-ray diffraction (XRD). More importantly, the work provides a basis for an in-depth understanding of the relationship between the microstructure and the electrochemical performance of the negative electrode material. These studies will provide further insight into the theoretical basis for the use of bi-based materials in SIBs.

Results and Discussion

The process for the preparation of N–C@Bi/G composites with a dual carbon encapsulated structure is shown in Figure 1, which consists of four steps: 1) in-situ growth of Bi_2O_3 nanoparticles on the surface of reduced graphene oxide (rGO), 2) in-situ polymerization of dopamine (DA) to synthesize PDA@ Bi_2O_3 /rGO composites, 3) introduction of graphene oxide (~20 wt%) to prepare PDA@ Bi_2O_3 /rGO gel, 4) heat treatment of PDA@ Bi_2O_3 /rGO to form N–C@Bi/G composites.

Morphology and detailed microstructure of N–C@Bi/G were studied by SEM and TEM. The SEM images of N–C@Bi/G in Figure 2(a) show a typical three-dimensional continuous porous network with no obvious large pores and a large number of uniformly sized N–C@Bi nanoparticles (about 78 nm) uniformly distributed on the graphene substrate while being encapsulated by graphene. In addition, the energy spectrum dispersion map (EDS) mapping images (Figure S1E1–E3) show that Bi, N and C are uniformly distributed in the N–C@Bi/G composites, indicating that the N–C@Bi nanoparticles are uniformly encapsulated in the graphene. High resolution transmission electron microscopy (HRTEM) images show that the N–C@Bi NPs are encapsulated by carbon layers $< 10 \text{ nm}$ in thickness (Figure 2c). Moreover, the interlayer distance of the N–C@Bi NPs is 0.32 nm, corresponding to the rhombic phase (012) plane of metallic Bi

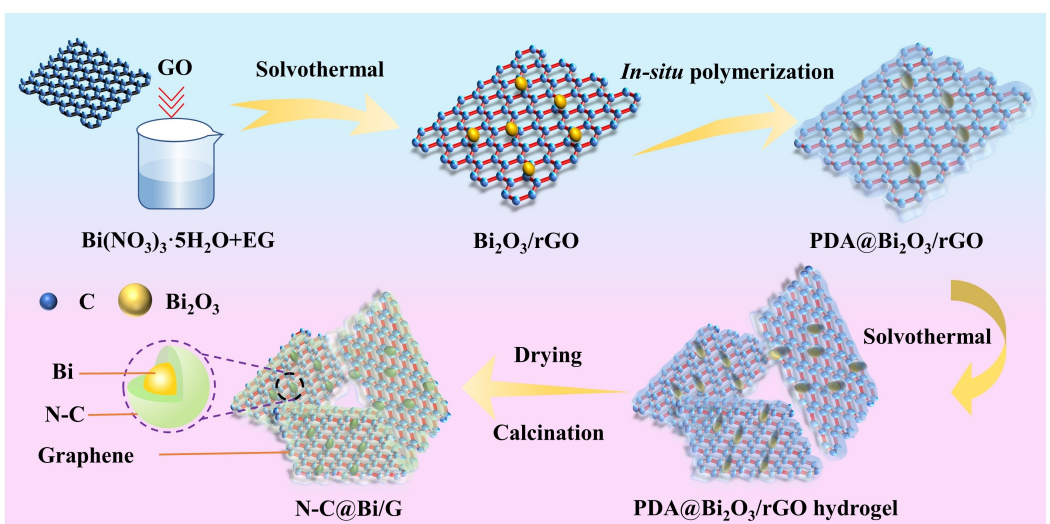


Figure 1. Schematic diagram of N–C@Bi/G synthesis.

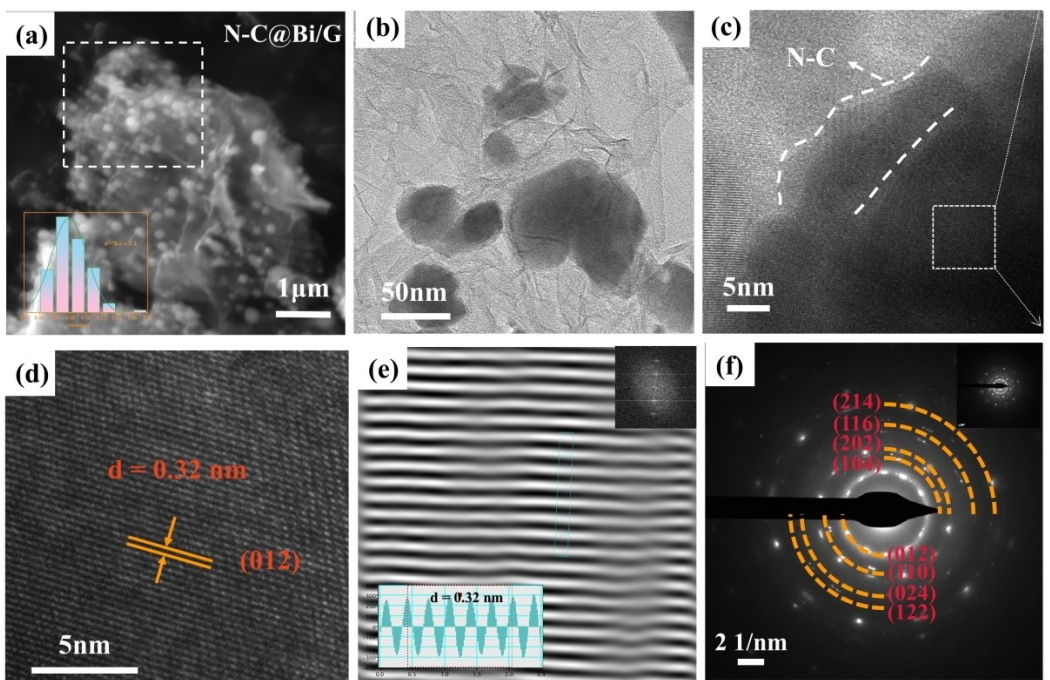


Figure 2. a) SEM; b, c) TEM; d) HRTEM images; e) inversed Fourier-transformed crystalline lattice form and f) SAED pattern of N–C@Bi/G.

(JCPDS 01-085-1331) (Figure 1c–e). Meantime, the corresponding selected area electron diffraction (SAED) pattern (Figure 2f) shows reflections attributed to the Bi phase ((012), (104), (110), (202), (024), (116), (122) and (214) faces of rhombic phase Bi), confirming the nanocrystalline nature of the selected area.

Powder X-ray diffraction (XRD) pattern further characterize the structure and composition of the N–C@Bi/G composites (Figure 3a). In Figure 3(a), the XRD pattern of Bi₂O₃@rGO shows extra peaks at around 25° and 40° belong to Bi (JCPDS No.44-1246), which is due to a small amount of Bi(NO₃)₃·5H₂O was completely reductive to Bi during the preparation of the precursor Bi₂O₃@rGO. After calcination in H₂/Ar atmosphere at 500°C, Bi₂O₃ was completely reduced to Bi. All of the peaks correspond well to Bi (JCPDS No.44-1246), and these sharp peaks indicate a high degree of crystallinity in the N–C@Bi/G composite. Although the carbon material cannot be directly detected in the XRD diagram, it can be clearly observed in the Raman spectrum (Figure 3f). The elemental content of the N–C@Bi/G composite was determined using thermogravimetric analysis (TGA) (Figure S4) and the Bi content was 64.2%.

Determination of the composition and valence of N–C@Bi/G composites by high resolution X-ray photoelectron spectroscopy (XPS). The composition and valence of the N–C@Bi/G, the results are shown in Figure 3(b).The elements Bi, N and C can be clearly observed in the full measurement spectrum. Bi 4f high resolution spectra are shown in Figure 3(c), with two main peaks at 159.4 eV (Bi 4f^{7/2}) and 164.7 eV (Bi 4f^{5/2}).^[17] As shown in Figure 3(d), strong peaks at 284.1, 285.2, 286.1 and 289.8 eV, belong to C–C, C–N, C–O and O=C=O, indicating a high degree of rGO reduction and a high degree of N–C doping. Furthermore, as shown in Figure 3(e), the high resolution N 1s spectra of the N–C@Bi/G composites also

indicate that the nitrogen has pyridine N, pyridine N and graphite-like N compositions with binding energies of 398.3, 399.5 and 400.8 eV, respectively, which also indicate that N is successfully doped.^[18] Quantitative analysis shows that the N content is measured to be about 2.84 % in the N–C@Bi/G composites. N-doped carbon can greatly increase electrical conductivity and increase the number of reactive sites on the surface, enabling rapid charge transfer and ion diffusion.^[19]

Using Raman and nitrogen adsorption and desorption isotherms studied the three-dimensional structures of N–C@Bi/G and Bi/G were studied (Figure 3f–i). As shown in Figure 3(f), the Raman spectrum has two characteristic peaks at 1341 and 1590 cm⁻¹, which belong to the D and g bands of carbon, respectively.^[20] The G-band and D-band are associated with oscillations of sp² hybridized carbon and disordered carbon, respectively. Outside, the intensity ratio of the D- to G-band (I_D/I_G) reflects the degree of defects, with a higher I_D/I_G ratio indicating more defects in the carbon. I_D/I_G for N–C@Bi/G and Bi/G are 1.076 and 0.923, respectively, and the partial graphitization of the nitrogen-doped carbon gives the composite a high electrical conductivity.^[17] At the same time, the introduction of nitrogen-doped carbon produced an increase in defects in the composites, a large number of external defects and active sites for sodium ion diffusion, which greatly improved the electrochemical properties of the composites. The porosity of N–C@Bi/G and Bi/G was investigated using nitrogen adsorption and desorption isotherms as shown in Figure 3(g–i). The isothermal curves of Bi/G (Figure 3g, blue curve) exhibit the combined characteristics of type II/IV^[21] isotherm curves with a specific surface area of 5.95 m² g⁻¹ and a specific pore volume of 0.073 cm³ g⁻¹, as detailed in Table S1 of the Supporting Information. According to density functional

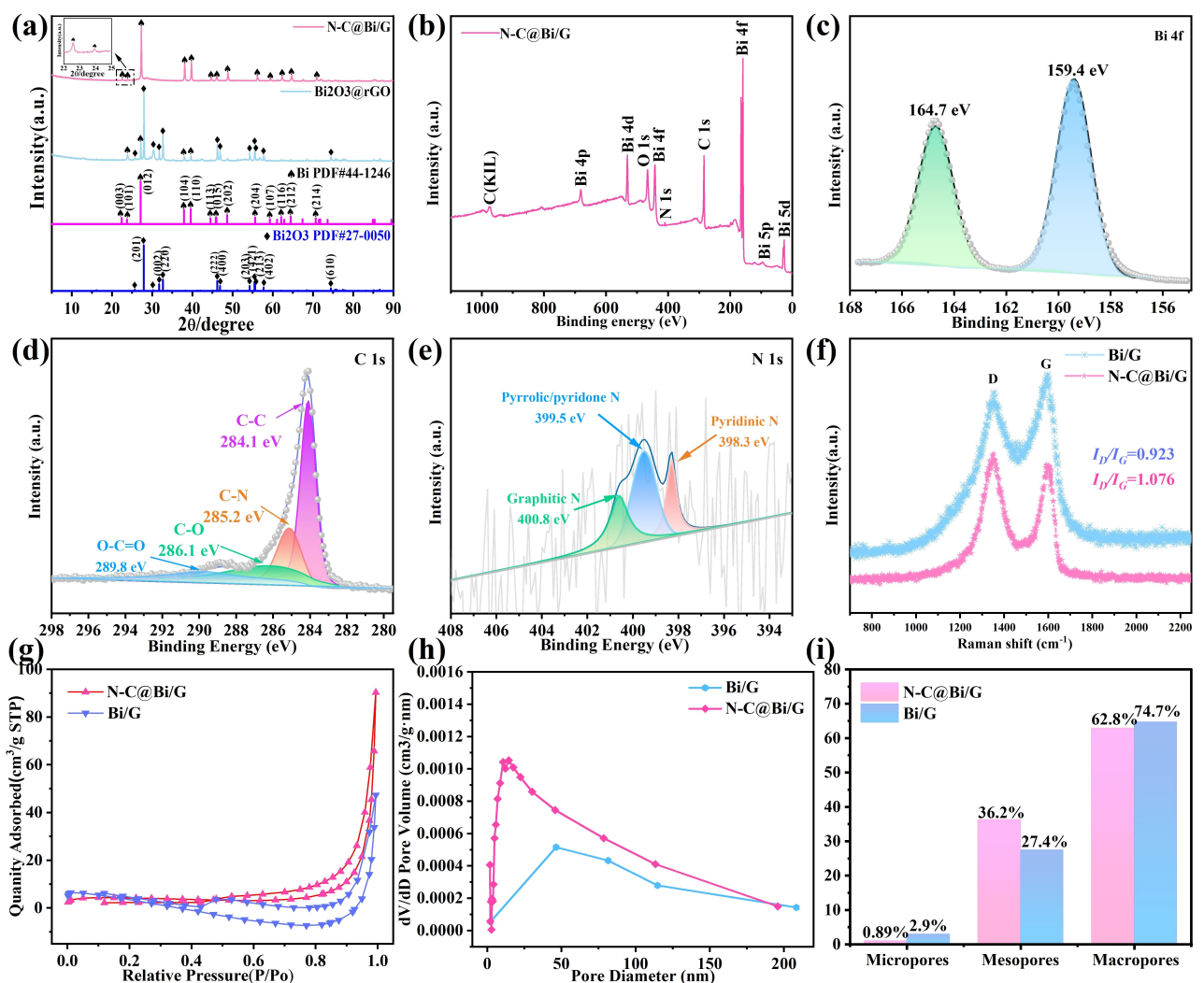


Figure 3. a) XRD patterns of the precursor Bi₂O₃@rGO and final composite N-C@Bi/G; b) XPS spectra of N-C@Bi/G; c) 4f spectrum of Bi; d) 1s spectrum of C; e) 1s spectrum of N; f) Raman diagram; g) nitrogen adsorption and desorption curves; h) comparison of pore structures and i) pore size distribution.

theory (DFT), the pore size distribution of Bi/G shows a rich hierarchical structure of small, meso, and large pores, the specific data are shown in the Table S1. The isotherm of N-C@Bi/G (Figure 3g) shows that the specific surface area of N-C@Bi/G is 12.30 m² g⁻¹, the specific pore volume is 0.14 cm³ g⁻¹, the pore size distribution ranging from 1 to 200 nm (Figure 3h). As can be seen from Figure 3(i), the specific surface area and specific pore volume of N-C@Bi/G are significantly larger compared to Bi/G, which indicates that the introduction of nitrogen-doped carbon enriches the pore structure of the material. And the developed pore structure with a larger specific surface area can provide more active sites to accelerate the ion transport and speed up the reaction kinetics.^[22]

The sodium storage performance of N-C@Bi/G composites was probed using assembled 2025 type half-cells in the voltage range of 0.01 to 2 V (vs. Na⁺/Na). Figure 4(a) shows three typical CV curves of N-C@Bi/G at 0.1 mVs⁻¹. In the first cycle, a small peak appears at 1.16 V, which the peak may be attributed to graphene by comparing the CV curves of N-C@Bi/G, Bi/G

(Figure S5a) and Bi (Figure S5b). A broad and weak cathodic peak appears at 0.62 V, due to the formation of the SEI layer and the alloying reaction of Bi→NaBi;^[23] in addition, A distinct small spike at 0.38 V appears, which corresponds to the alloying reaction of NaBi→Na₃Bi. In the subsequent negative process, two high spikes at 0.62 and 0.78 V, correspond to the two-step denaturation reaction of Na₃Bi→NaBi→Bi, respectively.^[24] In the second and third subsequent cycles, the CV curves for N-C@Bi/G largely overlap, but the redox peaks are sharper, showing excellent electrochemical reversibility and cycling stability. Figure 4(b) shows the corresponding constant current charge and discharge curves at 0.1 A g⁻¹, with the redox peaks matching the two plateaus and CV curves in the figure. The first week discharge capacity was 629.8 mAh g⁻¹, the charge capacity was 496.7 mAh g⁻¹ and the initial coulomb efficiency (ICE) was 78.87%. The irreversibility of the initial capacity loss can be attributed to the decomposition of the electrolyte to form the SEI layer and the side reactions between the carbon matrix and the electrolyte.^[25] The initial coulombic efficiency is higher than those of pure Bi (61.4%) and Bi/G (68.1%) anodes

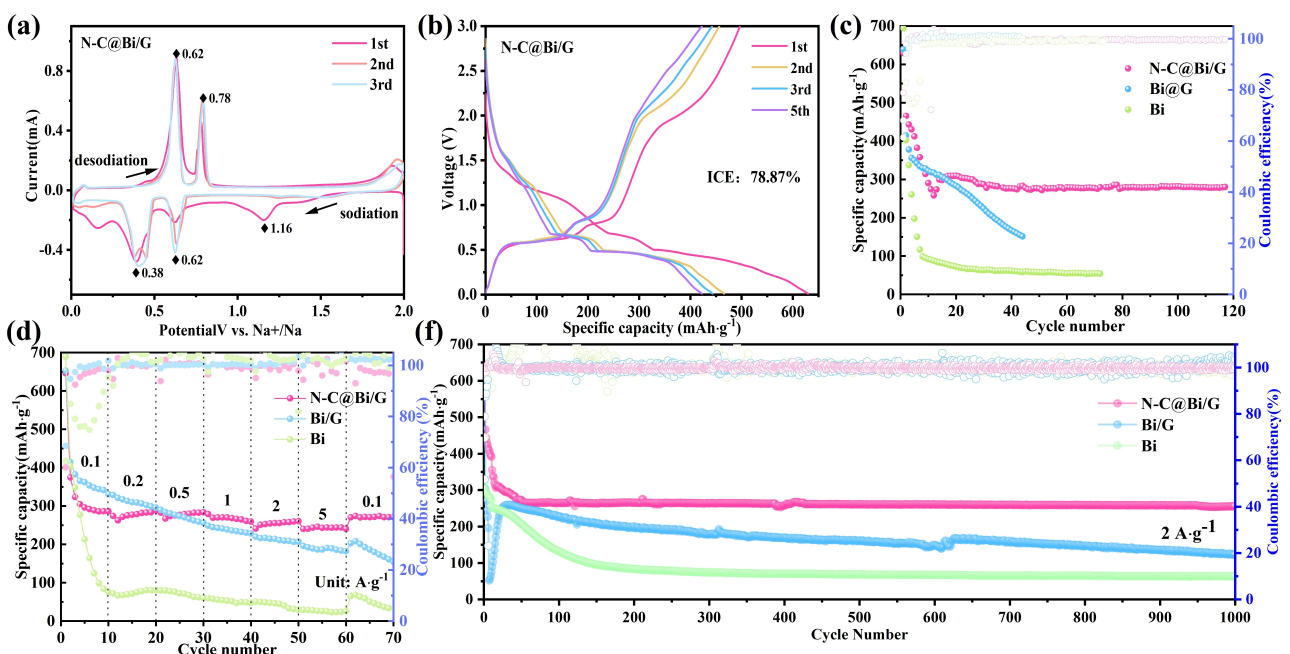


Figure 4. Sodium storage performance of N–C@Bi/G electrodes: a) CV curves at 0.1 mVs^{-1} , b) charge/discharge curves at 0.1 Ag^{-1} , c) cycling performance at 0.1 Ag^{-1} , d) rate performance, e) long-term cycling performance at 2.0 Ag^{-1} .

(Figure S5). In the following cycles, the coulombic efficiency (CE) rapidly increases to close to 100% with no significant change in the voltage profile, indicating that the irreversible reaction occurs only in the initial stage. As shown in Figure 4(c), the N–C@Bi/G anode electrode material can maintain a specific capacity of 280.1 mAh g^{-1} after 120 cycles at 0.1 Ag^{-1} current density, with a much higher stability than that of the Bi/G anode material under the same conditions. In addition, rate performance of the battery of N–C@Bi/G was tested at different current densities ($0.1\text{--}5 \text{ Ag}^{-1}$). As shown in Figure 4(d), a high specific capacity of 260.4 mAh g^{-1} was maintained when the current density was increased from 0.1 to 2 Ag^{-1} . Even at the very high current rate of 5 Ag^{-1} , a capacity of 246 mAh g^{-1} is still provided, with a significantly higher multiplicative performance than that of the Bi/G without nitrogen-doped carbon. As shown in Figure 4(e), the N–C@Bi/G anode electrode material can maintain a specific capacity of 257.6 mAh g^{-1} after 1000 cycles at 2 Ag^{-1} current density (Capacity retention is 87.7%), the electrochemical properties are significantly higher than those of pure Bi (26.6%) and Bi/G (48.9%). The improved performance of the N–C@Bi/G composites is related to the dual-encapsulated structure protection layer derived from N–C and G, which ensures fast kinetics but also suppresses the structural changes caused by volume expansion very well and improve the reversibility of the phase transition, thus contribute to improved reaction kinetics and achieve long-term cycle stability.

The kinetics of the N–C@Bi/G electrode reaction was further investigated using cyclic voltammetry (CV) at $0.1, 0.2, 0.4, 0.8$ and 1.0 mVs^{-1} voltage scan rates, respectively (Figure 5a). Theoretically, we can describe the relationship between the

peak current (i) and the voltage sweep rate (ν)^[26] using the following Equations (1) and (2):

$$i = a\nu^b \quad (1)$$

$$\log i = \log a + b \log \nu \quad (2)$$

Plotted with $\log \nu$ as the horizontal coordinate and $\log i$ as the vertical coordinate, the slope of the curve is the value of b . Diffusion dominated process as b approaches 0.5, pseudocapacitance behavior as b reaches 1. As Figure 5(b) shows, the b values of peak I, II, III and IV of N–C@Bi/G composites are 0.55, 0.56, 0.57 and 0.58, respectively, indicating that the sodium storage of the N–C@Bi/G composites is limited by diffusion processes and pseudocapacitance behavior, which is beneficial for improving the sodium storage performance. Figure 5(c) showed the contribution of pseudocapacitance at different scan speeds. Next, we used electrochemical impedance spectroscopy (EIS) to further explore the kinetic processes in the N–C@Bi/G composites. The equivalent circuit is shown in the inset of Figure 5(d), where R_{ct} represent the charge transfer resistance.^[27] Details are given in Table S2 of the Supporting Information. The R_{ct} of the N–C@Bi/G composites is 0.50Ω according to the Nyquist diagram, which is smaller than that of Bi/G (3.35Ω) and Bi (35.84Ω), conforming that N doped into the carbon matrix is beneficial to improve the rapid electron transfer during the charge/discharge process. Moreover, the σ values can be quantified based on the following Equations (3):

$$Z' = R_{ct} + R_e + \sigma \omega^{1/2} \quad (3)$$

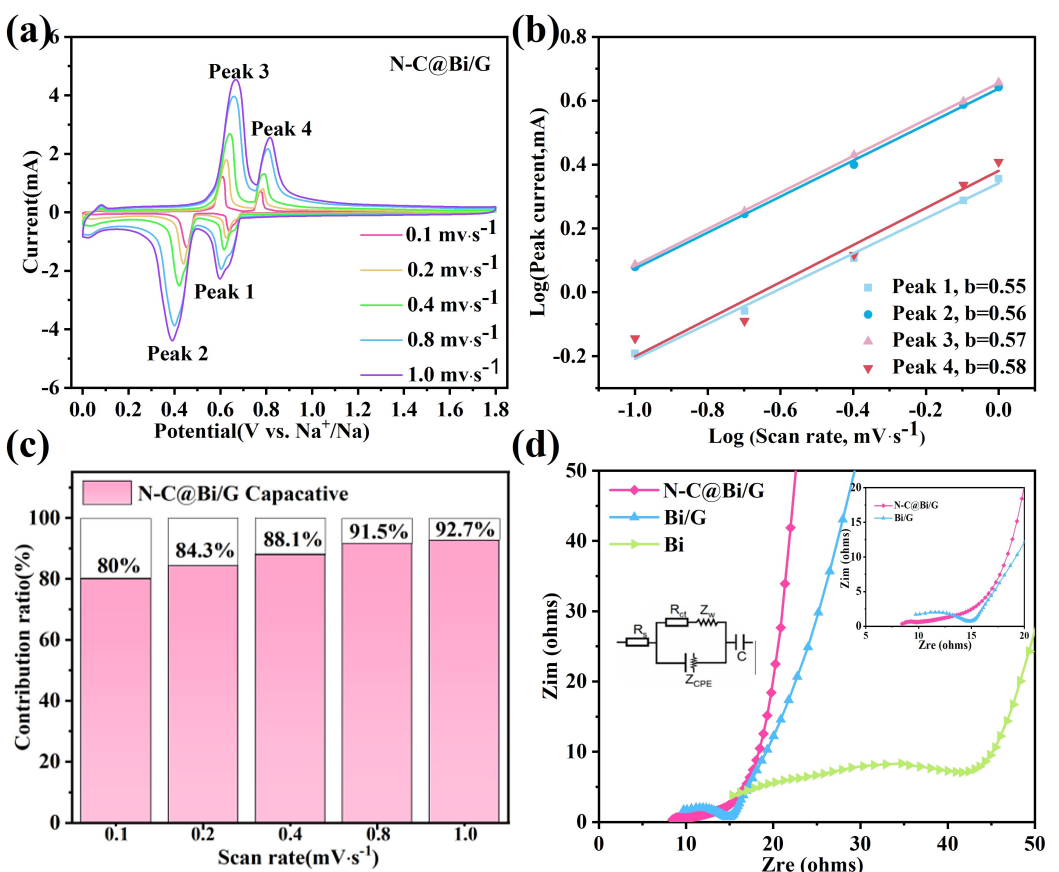


Figure 5. a) CV curves at different sweep rates (0.1 to 1) for N-C@Bi/G, b) b-value curves determined from the relationship between peak current and sweep rate for N-C@Bi/G, c) pseudocapacitance contribution and d) Nyquist plots for N-C@Bi/G, Bi/G and Bi.

The σ values of the N-C@Bi/G, Bi/G and pure-Bi electrodes are calculated to be 6.7, 23.3 and 119.5, respectively. It's obvious that the σ value of the N-C@Bi/G electrode is smaller than that of the pure Bi and Bi/G electrodes, indicating that the kinetic velocity of the N-C@Bi/G electrode is faster. The relationship between Z' and σ is plotted as shown in the Figure S7 and the detailed breakdown values are shown in the Table S2. Based on the above analysis, the introduction of the N-C layer can significantly reduce the charge transfer resistance and improve the sodium ion diffusion rate, thus improving the fast reaction kinetics, which can also explain why the N-C@Bi/G composites exhibit excellent electrochemical properties.

In addition, we characterized the sodium storage mechanism of the N-C@Bi/G electrode during the first lap cycle by in-situ XRD. The current density is $0.3 \mu\text{A}\text{g}^{-1}$ and the voltage ranges from 0.01 to 2.0 V (vs. Na^+/Na). The in-situ XRD pattern of N-C@Bi/G is shown in Figure 6. At the beginning of the first discharge, all peaks correspond well to the diffraction peaks of Bi. When the open circuit voltage (OCV) discharging from 2.0 to 0.6 V (vs. Na^+/Na) (the first voltage plateau, stage 1), the diffraction intensity of the characteristic peak of Bi continues to decrease and almost disappears. At the same time, new diffraction peaks appear at 25.7° , 31.9° , 36.7° and 41.4° , with a gradual increase in intensity. These new peaks belong to the

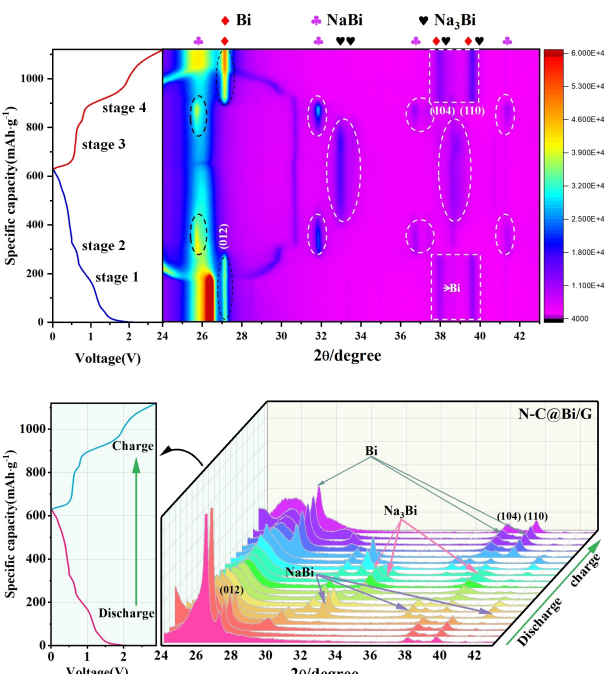
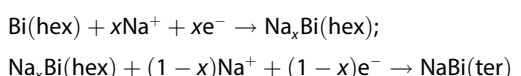


Figure 6. In situ XRD pattern of N-C@Bi/G.

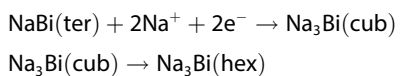
tetragonal NaBi phase (JCPDS NO. 65-8734), indicating the sodiation of bismuth in phase 1 as bismuth alloyed with sodium to form NaBi ($\text{Bi} \rightarrow \text{NaBi}$). It is noteworthy that at the beginning of phase 1 the Bi peaks are slightly shifted towards the lower 2θ angle, this suggests that the embedding of Na ions into the Bi lattice may have caused a change in the initial volume of Bi. During the 0.6–0.01 V (vs. Na^+/Na) (stage 2), the NaBi phase gradually disappears and new diffraction peaks start to appear at 32.8, 33.6, 38.0 and 39.2, which belong to the hexagonal Na_3Bi phase (JCPDS NO. 65-3525). At the end of the second voltage plateau, the final discharge product is a single Na_3Bi phase, which confirms the second stage of sodiation as the complete alloying of NaBi with Na^+ to form Na_3Bi ($\text{NaBi} \rightarrow \text{Na}_3\text{Bi}$).^[11,24]

In the first discharge process, there are two deformations of the N–C@Bi/G electrode occurs, corresponding to two flat voltage plateaus (phases 3 and 4, Figure 6). In the third stage (0.01–0.75 V vs. Na^+/Na), the diffraction peak of Na_3Bi gradually fades and eventually disappears, accompanied by the reappearance of the NaBi phase. Apparently, this phase is related to the denaturation of Na_3Bi to NaBi ($\text{Na}_3\text{Bi} \rightarrow \text{NaBi}$). Furthermore, as the denaturation proceeds (0.75–2.0 V vs. Na^+/Na), a double peak appears and continues to increase until the end of phase 4. At the same time, the NaBi phase is demineralized to form Bi ($\text{NaBi} \rightarrow \text{Bi}$) and disappears. The specific reactions are as follows:

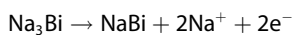
Stage 1.



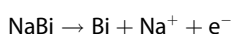
Stage 2.



Stage 3:



Stage 4:



The in-situ XRD results clearly confirm the alloying/dealloying mechanism and the good reversibility of the N–C@Bi/G electrode.

Conclusion

In summary, we have successfully prepared a highly reversible N–C@Bi/G composites of nitrogen-doped carbon and graphene bilayers coated with carbon by a two-step hydrothermal method and annealing treatment, and the N–C@Bi were uniformly distributed on the graphene base. As an anode material for SIBs, the N–C@Bi/G electrode exhibits rapid,

ultrahigh and durable sodium storage. It was found that N–C with abundant defects can provide more active sites for surface ion storage, reduce ion/electron diffusion pathways and improve reaction kinetics. The three-dimensionally interconnected conductive graphene network provides a larger surface for the dispersion of N–C@Bi nanoparticles, further facilitating electron transfer and ion diffusion over a larger space. Due to its unique structural advantage of double-layer carbon coating, the N–C@Bi/G composite exhibits excellent sodium storage performance with a capacity of 280 mAh g^{-1} at 0.1 A g^{-1} and an initial coulombic efficiency of 78.87%; At a current density of 2 A g^{-1} , a capacity of 260 mAh g^{-1} can still be obtained after 1000 cycles. More importantly, in-situ XRD can also confirm that the two carbon layers, N–C and G, not only reduce the electron/ion diffusion paths and ensure fast reaction kinetics. At the same time, the volume expansion caused by the two-step alloying ($\text{Bi} \leftrightarrow \text{NaBi} \leftrightarrow \text{Na}_3\text{Bi}$) of the electrode material during sodium storage process can be effectively mitigated and structural stability can be maintained. These results will provide important guidance for the development of bismuth-based anode materials.

Experimental Section

All chemicals including bismuth nitrate pentahydrate ($\text{Bi}(\text{NO}_3)_3 \cdot 5\text{H}_2\text{O}$, Aladdin), sodium borohydride (NaBH_4 , Aladdin), were used without further purification. Graphene oxide (GO) is prepared by a modified Hummers method.^[28]

Synthesis of $\text{Bi}_2\text{O}_3/\text{rGO}$ precursor: Add 0.433 g of $\text{Bi}(\text{NO}_3)_3 \cdot 5\text{H}_2\text{O}$ to 30 mL of GO suspension (1 mg/mL, sonicated for 1 h), sonicate and stir magnetically for 30 min; add 30 mL of ethylene glycol, sonicate and stir magnetically for 30 min, add 0.3 g of NaBH_4 to the above mixture, then transfer to a 100 mL hydrothermal kettle and hold at 180 °C for 10 h. After cooled, the product was washed with anhydrous ethanol and deionized water alternately and dried by centrifugation for 6 h to obtain $\text{Bi}_2\text{O}_3/\text{rGO}$.

Synthesis of PDA@ $\text{Bi}_2\text{O}_3/\text{rGO}$: $\text{Bi}_2\text{O}_3/\text{rGO}$ was added to Tris buffer solution ((0.121 g Tris in 100 mL water), followed by an appropriate amount of DA, stirred for 24 h, washed and dried by centrifugation for 6 h to obtain PDA@ $\text{Bi}_2\text{O}_3/\text{rGO}$ black powder. The PDA@ $\text{Bi}_2\text{O}_3/\text{rGO}$ powder was dispersed in 30 mL deionized water with 30 mL GO suspension (2 mg/mL), transferred to a 100 mL hydrothermal kettle for 6 h at 180 °C, washed and dried to obtain PDA@ $\text{Bi}_2\text{O}_3/\text{rGO}$ gel.

Synthesis of N–C@Bi/G: The PDA@ $\text{Bi}_2\text{O}_3/\text{rGO}$ gel was placed in a tube furnace with a mixed H_2/Ar atmosphere and heated up to 450 °C at 5 °C min⁻¹, then calcined at 450 °C for 2 h and brought to room temperature at 10 °C min⁻¹ to obtain N–C@Bi/G.

Material characterization: The crystalline composition of the material was determined using an X-ray diffractometer (XRD) (Rigaku Smartlab SE), diffracted using Cu target K_α rays ($\lambda = 1.5406 \text{ \AA}$). The microscopic morphology and structure were characterized using scanning electron microscopy (SEM, MiRA3-LMM) and transmission electron microscopy (TEM, JEM-2100F). The chemical state of the sample surface was analyzed by X-ray photoelectron spectroscopy (XPS) (Thermo Kalpha). Thermogravimetric analysis (TGA) of the samples was carried out in air using a NETZSCH STA 449F5 with a temperature rise rate of 10 °C min⁻¹. The samples were analysed using a Micromeritics ASAP 2460. The samples were

tested for nitrogen adsorption and desorption at 77 K using a Micromeritics ASAP 2460 device. Particle size distribution was analyzed by Nano Measurer 1.2 software.

Electrochemical testing: The electrodes were made by assembling a 2025 type button half-cell with a sodium sheet as counter electrode. The electrodes were made by the prepared active material (80% N–C@Bi/G), Super P(10%), and Polyvinylidene fluoride (10%). The electrochemical performance of the cells was tested at 0.01–2.0 V using a LAND cell test system (LAND CT-2001A, China). The step-cycle voltammetric curves of the cells were tested using an electrochemical workstation (PARSTAT PMC1000, America) at a sweep rate of 0.1 mV s⁻¹. Electrochemical impedance spectra (EIS) were also obtained from the above equipment in the frequency range of 100 kHz to 0.01 Hz.

Acknowledgements

This work has been supported by the National Natural Science Foundation of China (Grant No. 52072256), Shanxi Science and Technology Major Project (Grant No. 20201101016 and 20181102019), Key R & D program of Shanxi Province (202102030201006), Research Project Supported by Shanxi Scholarship Council of China (HGKY2019031), Natural Science Foundation of Shanxi Province (No. 20210302124308).

Conflict of Interest

The authors declare no conflict of interest.

Data Availability Statement

Research data are not shared.

Keywords: bismuth double carbon layer · nitrogen doping · rapid reaction kinetics · sodium-ion batteries

- [1] a) Z. Wu, Y. Wang, X. Liu, C. Lv, Y. Li, D. Wei, Z. Liu, *Adv. Mater.* **2019**, *31*, e1800716; b) J. Zhao, J. Lian, Z. Zhao, X. Wang, J. Zhang, *Nano-Micro Lett.* **2022**, *15*, 19.
- [2] a) X. Zhou, L. J. Wan, Y. G. Guo, *Adv. Mater.* **2013**, *25*, 2152–2157; b) J. Xu, Y. Xu, C. Lai, T. Xia, B. Zhang, X. Zhou, *Sci. China Chem.* **2021**, *64*, 1267–1282; c) Z. Zhao, Y. Duan, F. Chen, Z. Tian, R. Pathak, J. W. Elam, Z. Yi, Y. Wang, X. Wang, *Chem. Eng. J.* **2022**, *450*.
- [3] a) C. Zhao, F. Ding, Y. Lu, L. Chen, Y. S. Hu, *Angew. Chem. Int. Ed. Engl.* **2020**, *59*, 264–269; b) C. Zhao, Z. Yao, Q. Wang, H. Li, J. Wang, M. Liu, S. Ganapathy, Y. Lu, J. Cabana, B. Li, X. Bai, A. Aspuru-Guzik, M. Wagemaker, L. Chen, Y. S. Hu, *J. Am. Chem. Soc.* **2020**, *142*, 5742–5750.
- [4] a) M. Gu, A. M. Rao, J. Zhou, B. Lu, *Energy Environ. Sci.* **2023**, *16*, 1166–1175; b) Y. Hu, L. Fan, A. M. Rao, W. Yu, C. Zhuoma, Y. Feng, Z. Qin, J. Zhou, B. Lu, *Natl. Sci. Rev.* **2022**, *9*, nwac134; c) L. Fan, H. Xie, Y. Hu, Z. Caixiang, A. M. Rao, J. Zhou, B. Lu, *Energy Environ. Sci.* **2023**, *16*, 305–315.
- [5] a) Y. Du, Z. Zhang, Y. Xu, J. Bao, X. Zhou, *Acta Phys. Chim. Sin.* **2022**, *38*, 2205017–2205010; b) Y. Du, Z. Yi, B. Chen, J. Xu, Z. Zhang, J. Bao, X.

Zhou, *J. Energy Chem.* **2022**, *66*, 413–421; c) X. Cheng, Q. Bai, H. Li, H. Dou, Z. Zhao, D. Bian, X. Wang, *Chem. Eng. J.* **2022**, *442*, 136222; d) H. Che, S. Chen, Y. Xie, H. Wang, K. Amine, X.-Z. Liao, Z.-F. Ma, *Energy Environ. Sci.* **2017**, *10*, 1075–1101.

- [6] J. Sun, P. Edenborg, H. Grönbeck, P. H. Thiesen, Z. Xia, V. Quintano, R. Qiu, A. Matic, V. Palermo, *Sci. Adv.* **2021**, *7*, eabf0812.
- [7] a) X. Sun, L. Wang, C. Li, D. Wang, I. Sikandar, R. Man, F. Tian, Y. Qian, L. Xu, *Nano Res.* **2021**, *14*, 4696–4703; b) J. Ni, X. Li, M. Sun, Y. Yuan, T. Liu, L. Li, J. Lu, *ACS Nano* **2020**, *14*, 9117–9124; c) Y. V. Lim, X. L. Li, H. Y. Yang, *Adv. Funct. Mater.* **2020**, *31*, 2006761.
- [8] a) L. Fang, N. Bahlawane, W. Sun, H. Pan, B. B. Xu, M. Yan, Y. Jiang, *Small* **2021**, *17*, e2101137; b) K. Song, C. Liu, L. Mi, S. Chou, W. Chen, C. Shen, *Small* **2021**, *17*, e1903194.
- [9] a) B. Xu, S. Qi, P. He, J. Ma, *Chem. Asian J.* **2019**, *14*, 2925–2937; b) H. Gao, J. Niu, C. Zhang, Z. Peng, Z. Zhang, *ACS Nano* **2018**, *12*, 3568–3577.
- [10] a) D. Su, S. Dou, G. Wang, *Nano Energy* **2015**, *12*, 88–95; b) Y. Qin, Y. Zhang, J. Wang, J. Zhang, Y. Zhai, H. Wang, D. Li, *ACS Appl. Mater. Interfaces* **2020**, *12*, 42902–42910; c) K. Lei, C. Wang, L. Liu, Y. Luo, C. Mu, F. Li, J. Chen, *Angew. Chem. Int. Ed. Engl.* **2018**, *57*, 4687–4691.
- [11] Z. Hu, X. Li, J. Qu, Z. Zhao, H. Xie, H. Yin, *J. Power Sources* **2021**, *496*, 229830.
- [12] a) H. Yang, R. Xu, Y. Yao, S. Ye, X. Zhou, Y. Yu, *Adv. Funct. Mater.* **2019**, *29*, 1809195; b) Z. Sun, Y. Liu, W. Ye, J. Zhang, Y. Wang, Y. Lin, L. Hou, M. S. Wang, C. Yuan, *Angew. Chem. Int. Ed.* **2021**, *60*, 7180–7187; *Angew. Chem.* **2021**, *133*, 7256–7263.
- [13] a) X. Wu, Y. Chen, Z. Xing, C. W. K. Lam, S. S. Pang, W. Zhang, Z. Ju, *Adv. Energy Mater.* **2019**, *9*, 1900343; b) J. Zheng, Y. Wu, Y. Tong, X. Liu, Y. Sun, H. Li, L. Niu, *Nano-Micro Lett.* **2021**, *13*, 174.
- [14] a) H. Long, X. Yin, X. Wang, Y. Zhao, L. Yan, *J. Energy Chem.* **2022**, *67*, 787–796; b) L. Wang, B. Zhang, B. Wang, S. Zeng, M. Zhao, X. Sun, Y. Zhai, L. Xu, *Angew. Chem. Int. Ed. Engl.* **2021**, *60*, 15381–15389.
- [15] F. Yang, F. Yu, Z. Zhang, K. Zhang, Y. Lai, J. Li, *Chem.* **2016**, *22*, 2333–2338.
- [16] Y. Liang, N. Song, Z. Zhang, W. Chen, J. Feng, B. Xi, S. Xiong, *Adv. Mater.* **2022**, *34*, e2202673.
- [17] P. Xue, N. Wang, Z. Fang, Z. Lu, X. Xu, L. Wang, Y. Du, X. Ren, Z. Bai, S. Dou, G. Yu, *Nano Lett.* **2019**, *19*, 1998–2004.
- [18] Y. Li, C. Ou, J. Zhu, Z. Liu, J. Yu, W. Li, H. Zhang, Q. Zhang, Z. Guo, *Nano Lett.* **2020**, *20*, 2034–2046.
- [19] X. Wang, Y. Wu, P. Huang, P. Chen, Z. Wang, X. Xu, J. Xie, J. Yan, S. Li, J. Tu, Y. L. Ding, *Nanoscale* **2020**, *12*, 23682–23693.
- [20] a) Y. Zhang, N. Wang, C. Sun, Z. Lu, P. Xue, B. Tang, Z. Bai, S. Dou, *Chem. Eng. J.* **2018**, *332*, 370–376; b) W. Hong, P. Ge, Y. Jiang, L. Yang, Y. Tian, G. Zou, X. Cao, H. Hou, X. Ji, *ACS Appl. Mater. Interfaces* **2019**, *11*, 10829–10840.
- [21] J. Z. Ryu, M. Wang, B. Zhang, *Carbon* **1999**, *37*, 1257–1264.
- [22] H. Li, X. Wang, Z. Zhao, R. Pathak, S. Hao, X. Qiu, Q. Qiao, *J. Mater. Sci. Technol.* **2022**, *99*, 184–192.
- [23] H. Dou, X. Zhao, Y. Zhang, W. Zhao, Y. Yan, Z.-F. Ma, X. Wang, X. Yang, *Nano Energy* **2021**, *86*, 106087.
- [24] C. Hu, Y. Zhu, G. Ma, F. Tian, Y. Zhou, J. Yang, Y. Qian, *Electrochim. Acta* **2021**, *365*, 137379.
- [25] H. Yang, L. W. Chen, F. He, J. Zhang, Y. Feng, L. Zhao, B. Wang, L. He, Q. Zhang, Y. Yu, *Nano Lett.* **2020**, *20*, 758–767.
- [26] L. Zhou, K. Zhang, J. Sheng, Q. An, Z. Tao, Y.-M. Kang, J. Chen, L. Mai, *Nano Energy* **2017**, *35*, 281–289.
- [27] S. Zhang, G. Wang, B. Wang, J. Wang, J. Bai, H. Wang, *Adv. Funct. Mater.* **2020**, *30*, 2001592.
- [28] W. S. Hummers, R. E. Offeman, *J. Am. Chem. Soc.* **1958**, *80*, 1339–1339.

Manuscript received: February 15, 2023
Revised manuscript received: March 14, 2023
Accepted manuscript online: March 19, 2023
Version of record online: March 29, 2023